The Astrophysical Journal, 998:306 (12pp), 2026 February 20
https://doi.org/10.3847/1538-4357/ae3a7d

A JWST Paα Calibration of the Radio Luminosity–Star Formation Rate Relation at $z \sim 1.3$

Nick Seymour[1], Catherine Hale[2,3], Imogen Whittam[2,4], Pascal Oesch[5,6], Alba Covelo-Paz[7], Stijn Wuyts[8], J. Afonso[9], R. A. A. Bowler[10], Joe Arthur Grundy[1], Ravi Jaiswar[1], Matt Jarvis[2,4], Allison Matthews[11], Romain A. Meyer[7], Chloe Neufeld[12], Naveen A. Reddy[13], Irene Shivaei[14], Dan Smith[15], Rohan Varadaraj[2], Michael A. Wozniak[16], and Lyla Jung[2]

[1] International Centre for Radio Astronomy Research, Curtin University, GPO Box U1987, Bentley, WA 6845, Australia
[2] Astrophysics, Department of Physics, University of Oxford, Keble Road, Oxford, OX1 3RH, UK
[3] Institute for Astronomy, University of Edinburgh, Royal Observatory Edinburgh, Blackford Hill, Edinburgh, EH9 3HJ, UK
[4] Department of Physics & Astronomy, University of the Western Cape, Private Bag X17, Bellville, Cape Town, 7535, South Africa
[5] Department of Astronomy, University of Geneva, Chemin Pegasi 51, CH-1290 Versoix, Switzerland
[6] Cosmic Dawn Center (DAWN), Niels Bohr Institute, University of Copenhagen, Jagtvej 128, DK-2200 København N, Denmark
[7] Department of Astronomy, University of Geneva, Chemin Pegasi 51, 1290 Versoix, Switzerland
[8] Department of Physics, University of Bath, Claverton Down, Bath, BA2 7AY, UK
[9] Instituto de Astrofísíca e Ciências do Espaço, Faculdade de Ciências, Universidade de Lisboa, OAL, Tapada da Ajuda, PT1349-018 Lisboa, Portugal
[10] Jodrell Bank Centre for Astrophysics, Department of Physics and Astronomy, School of Natural Sciences, The University of Manchester, Manchester, M13 9PL, UK
[11] Carnegie Observatories, 813 Santa Barbara Street, Pasadena, CA 91101, USA
[12] Astronomy Department, Yale University, 52 Hillhouse Avenue, New Haven, CT 06511, USA
[13] Department of Physics & Astronomy, University of California, Riverside, CA 92521, USA
[14] Centro de Astrobiología (CAB), CSIC-INTA, Carretera de Ajalvir km 4, Torrejón de Ardoz, 28850, Madrid, Spain
[15] Centre for Astrophysics Research, Department of Physics, Astronomy and Mathematics, University of Hertfordshire, Hatfield AL10 9AB, UK
[16] Department of Physics and Astronomy, University of California, Riverside, 900 University Avenue, Riverside, CA 92521, USA

Received 2025 September 3; revised 2025 December 23; accepted 2026 January 15; published 2026 February 18

Abstract

As radio emission from normal galaxies is a dust-free tracer of star formation, tracing the star formation history of the Universe is a key goal of the Square Kilometre Array and the Next-Generation Very Large Array. In order to investigate how well radio luminosity traces star formation rate (SFR) in the early Universe, we have examined the radio properties of a JWST Paα sample of galaxies at $1.0 \lesssim z \lesssim 1.8$. In the GOODS-S field, we cross-matched a sample of 506 FRESCO Paα emitters with the 1.23 GHz radio continuum data from the MeerKAT MIGHTEE survey, finding 47 detections. After filtering for active galactic nuclei (via X-ray detections, hot mid-infrared dust, and extended radio emission), as well as blended sources, we obtained a sample of star-forming galaxies comprising 11 cataloged radio detections, 18 noncataloged detections (at $\approx 3\sigma$–5σ), and 298 undetected sources. Stacking the 298 undetected sources, we obtain a 3.3σ detection in the radio. This sample, along with a local sample of Paα emitters, lies along previous radio luminosity/SFR relations from local (<0.2) to high redshift ($z \sim 1$). Fitting the FRESCO data at $1.0 \lesssim z \lesssim 1.8$, we find $\log(L_{1.4\mathrm{GHz}}) = (1.31 \pm 0.17) \times \log(\mathrm{SFR}_{\mathrm{Pa}\alpha}) + (21.36 \pm 0.17)$, which is consistent with other literature relations. We can explain some of the observed scatter in the $L_{1.4\mathrm{GHz}}/\mathrm{SFR}_{\mathrm{Pa}\alpha}$ correlation by a toy model in which the synchrotron emission is a delayed/averaged tracer of the instantaneous Paα SFR by ∼10/75 Myr.

Unified Astronomy Thesaurus concepts: Extragalactic radio sources (508); Galaxy evolution (594); Starburst galaxies (1570)

1. Introduction

Radio emission from normal galaxies, i.e., those without active galactic nuclei (AGN), has long been heralded as an unbiased tracer of star formation, one not affected by gas or dust. Emission at radio frequencies is dominated by synchrotron processes from relativistic electrons and free–free processes from thermal electrons (see review by J. J. Condon 1992). The relativistic electrons are thought to be accelerated by shocks from supernovae, which only come from massive OB stars ($>8\,M_\odot$; R. C. Kennicutt & N. J. Evans 2012), and then gyrate in the galactic magnetic field, whereas the thermal electrons are heated by the same bright stars in H II regions. This framework explains the well-established radio/far-infrared (far-IR) luminosity correlation (M. Harwit & F. Pacini 1975; J. J. Condon et al. 1991; M. S. Yun et al. 2001) observed for star-forming galaxies (SFGs) in the local Universe. The far-IR bump is also directly connected to star formation owing to interstellar dust thermally reradiating absorbed UV/optical emission from star-forming regions. Hence, the calibration between radio luminosity to star formation rate (SFR) was first derived from the radio/far-IR correlation (e.g., R. C. Kennicutt 1998; E. F. Bell 2003).

Deep radio surveys probing below ∼1 mJy have long shown an upturn in the source counts at faint flux densities (e.g., R. A. Windhorst et al. 1984; N. Seymour et al. 2004), which has been shown to be due to a population of distant SFGs. While robustly distinguishing between radio emission from an SFG or AGN remains an issue (H. S. B. Algera et al. 2020), deep radio surveys are now routinely used to measure the star formation history (SFH) of the Universe (N. Seymour et al. 2008; M. Novak et al. 2017; R. K. Cochrane et al. 2023).

Furthermore, the radio/far-IR correlation has been shown to extend to high redshifts ($z > 1$; R. J. Ivison et al. 2010), demonstrating that radio luminosity can trace SFR at high z well, albeit with some potential evolution (B. Magnelli et al. 2015; J. Delhaize et al. 2017; M. Bonato et al. 2021; I. Delvecchio et al. 2021). Some work has been performed using dust-corrected Hα emission lines at $1.4 < z < 2.6$ (K. J. Duncan et al. 2020), which found that the SFR/radio luminosity relation at this epoch was consistent with that found locally. The measurement of the radio-derived SFH has been determined from broad and deep source counts, as well as confusion $P(D)$ analysis probing source counts below the detection limit (A. M. Matthews et al. 2021), including radio emission potentially emitted up to $z \sim 6$. The culmination of this work was the adoption by the Square Kilometre Array (SKA) and the Next-Generation Very Large Array (ngVLA) of the key science goal of "probing galaxy evolution in the radio continuum" (I. Prandoni & N. Seymour 2015; M. Jarvis et al. 2015; E. Murphy et al. 2019).

Despite this promise, there remain some complications in straightforwardly using radio luminosities as a tracer of SFR. First, the broad radio spectrum (0.05–50 GHz) is not always a simple power law, as different frequency regimes sample different physical processes. While the thermal free–free emission dominates at high frequencies with a spectral index of $\alpha \sim -0.1$ (where the flux density $S_\nu \propto \nu^\alpha$ across frequency ν), the nonthermal synchrotron emission dominates at lower frequencies with $\alpha \sim -0.8$, around 1 GHz. In addition to the spectral flattening at higher frequencies as the thermal emission begins to dominate, there has long been evidence for low-frequency turnovers (E. Hummel 1991; M. S. Clemens et al. 2010; T. J. Galvin et al. 2018; J. A. Grundy et al. 2025), due to free–free absorption, and also evidence for spectral breaks in the synchrotron emission at 1–10 GHz (M. S. Clemens et al. 2010; T. J. Galvin et al. 2018; S. Dey et al. 2022, 2024). These variations on the radio spectra are on top of varying thermal fractions (TFs; ~1%–15%; T. J. Galvin et al. 2018; S. Dey et al. 2022).

Second, there is the issue of timescales, with the free–free emission being directly related to the number of ionizing photons (with little dependence on temperature), making it a very immediate tracer of the current SFR. Synchrotron emission is likely a delayed tracer of SFR for two reasons: (1) it takes 10–30 Myr for the massive stars to go supernova (thereby producing the relativistic electrons that have been shock-accelerated by Type II supernovae), and (2) the typical lifetime of synchrotron-emitting electrons in a galaxy with a magnetic field of $B = 5\,\mu$G is around 100 Myr (J. J. Condon 1992), although the field in star-forming regions and nuclei can be higher ($B = 10$–$16\,\mu$G and $B = 30\,\mu$G, respectively; E. J. Murphy et al. 2011). Third, there is the issue of inverse Compton (IC) processes depressing the radio emission of SFGs at higher redshifts (e.g., I. H. Whittam et al. 2025 found a decrease in the radio emission of $3 < z < 5$ Lyman break galaxies consistent with IC losses). Hence, in the era of the SKA and ngVLA, there is a clear need to ensure that calibration of the radio-luminosity-to-SFR conversion is robust.

The Paα line is known as a superb tracer of SFR (e.g., A. Alonso-Herrero et al. 2006), like other optical and UV recombination lines. While it is weaker than the Balmer Hα line at 0.6563 μm, which is widely adopted as an SFR tracer, it has the advantage that its near-IR wavelength of 1.8756 μm means that it suffers a lot less from dust attenuation. However, this rest-frame wavelength lies between J and H band, where water vapor decreases the atmospheric transmittance, making ground-based observations very difficult (K. Tateuchi et al. 2015). Hence, the limited studies with Paα have either targeted redshifted galaxies (e.g., G. J. Hill et al. 1996; H. Falcke et al. 1998; D. Kim et al. 2010) and redshifted ULIRGs (e.g., T. W. Murphy et al. 1999), or have used space-based observations. The Near Infrared Camera and Multi-object Spectrometer (NICMOS) on the Hubble Space Telescope (HST) undertook several Paα studies in the local Universe (e.g., A. Alonso-Herrero et al. 2006; G. Liu et al. 2013), but due to the high angular resolution of HST, these observations were insensitive to diffuse Paα emission. Hence, such observations could not reliably obtain total Paα fluxes in the local Universe.

SKA precursors (e.g., MeerKAT) and pathfinders (e.g., eVLA, eMERLIN) are now producing surveys around 1 GHz with rms sensitivities $\lesssim 1\,\mu$Jy, producing catalogs likely to be dominated by high-z SFGs (D. van der Vlugt et al. 2021; C. L. Hale et al. 2025). At the same time, JWST has the sensitivity and wavelength coverage to detect Paα at $z > 1$ (e.g., C. Neufeld et al. 2024). Indeed, several studies have looked at the combination of Paschen and Balmer lines to study dust attenuation in JWST-selected galaxies (N. A. Reddy et al. 2023, 2025; Z. Liu et al. 2024; B. Lorenz et al. 2025) in the early Universe. In this work, we investigate the correlation between radio and Paα luminosity in order to verify current radio luminosity/SFR calibrators. In Section 2 we present the data used, which we analyze in Section 3. Our results are presented and discussed in Section 4, and we provide conclusions in Section 5. We assume a flat Λ cold dark matter (ΛCDM) cosmology with $\Omega_M = 0.3$, $\Omega_\Lambda = 0.7$, and $H_0 = 70\ \mathrm{km\,s^{-1}\,Mpc^{-1}}$.

2. Data

2.1. FRESCO Paα

The First Reionisation Epoch Spectroscopic Complete Observations (FRESCO) survey (Cycle 1 GO-1895; P. A. Oesch et al. 2023) is a Cycle 1 JWST program targeting ~60 arcmin^2 in each GOODS field with two 2×4 NIRCam/grism mosaics and with the F444W filter covering 3.8–5.0 μm and reaching 5σ line flux limits of $\sim 2 \times 10^{-18}\ \mathrm{erg\,s^{-1}\,cm^{-2}}$. The slitless/grism data were processed by `grizli`[17] in the same way as presented in C. Neufeld et al. (2024) and A. Covelo-Paz et al. (2025). Sources were preselected based on their photometric redshifts, before their continuum-subtracted spectra were extracted and redshifts identified with `grizli`. These identifications were visually inspected for possible contamination or misclassification. Full details on the FRESCO emission-line catalogs will be presented in A. Covelo-Paz et al. (2026, in preparation). All the JWST data used in this paper can be found on the MAST website.

Here we use the GOODS-South catalog of Paα line detections with 506 sources across $1.0 \lesssim z \lesssim 1.8$ ($\langle z \rangle \sim 1.3$) selected to be $>4\sigma$ and described in C. Neufeld et al. (2024). Two of these sources have broad lines with FWHM $> 1000\ \mathrm{km\,s^{-1}}$ (Y. Sun et al. 2025). Modeling of the spectral

---

[17] https://github.com/gbrammer/grizli/

energy distribution (SED) of the full sample over 0.4–8.0 μm with `Bagpipes` (A. C. Carnall et al. 2018) provides the usual galaxy properties of visual attenuation A_V (using the D. Calzetti et al. 2000, reddening curve), stellar mass, SED-fitted SFR, and mass-weighted stellar age. `BAGPIPES` uses the G. Bruzual & S. Charlot (2003) stellar population models and has a variable metallicity (with best fits for this sample generally around half of solar). We use the A_V to correct the mildly dust-obscured Paα flux densities. To do so, we assume that the nebular attenuation $A_V^{\rm neb} = A_V^{\rm cont}/0.44$, where $A_V^{\rm cont}$ is the attenuation of the stellar continuum (D. Calzetti 1997), a result confirmed by M. I. Arnaudova et al. (2025). While there is some scatter in the ratio between nebular and stellar attenuation (e.g., Y. Koyama et al. 2018), choosing extreme values causes the correction factor below to change by <0.1 dex. We also assume that the (nebular) Paα attenuation is $A_{{\rm Pa}\alpha}^{\rm neb} = A_V^{\rm neb}/6.97$ using the D. Calzetti et al. (2000) reddening curve with $R_V = 4.05$. Again, varying the choice of reddening curves only changes the correction factor by up to 0.1–0.2 dex. Hence, the final multiplicative correction factor to the Paα flux densities and luminosities is $10^{0.4\,A_V^{\rm cont}/(0.44\times6.97)}$. The mean value of this correction factor was 1.18, very similar to that estimated by C. Neufeld et al. (2024) via a different method.[18] Note that if we assume $A_V^{\rm neb} = A_V^{\rm cont}/0.44$, then the mean correction factor becomes 1.07, but the final radio luminosity/SFR correlation in Section 4 is negligibly affected, so the relationship between the stellar and gas attenuation does not have an effect on these results. The uncertainties on the Paα luminosities include both the measured flux uncertainty and that estimated for the A_V.

We derive SFRs from the dust-corrected Paα luminosities. These SFRs are an instantaneous measurement, as they arise from the nebulae directly illuminated by the most recently formed stars. We use the same conversion factor as C. Neufeld et al. (2024):

$$\frac{{\rm SFR}_{{\rm Pa}\alpha}}{M_\odot\ {\rm yr}^{-1}} = 4.6\times10^{-41}\times\frac{L_{{\rm Pa}\alpha}}{{\rm erg\ s}^{-1}}, \tag{1}$$

which assumes case B recombination (D. Osterbrock 1989), an electron temperature of 10^4 K, a Chabrier initial mass function (IMF; G. Chabrier 2003), and an intrinsic Hα-to-Paα ratio of 8.575 (this value can vary by $\sim\pm10\%$ depending on electron temperature). This calibration ultimately comes from E. J. Murphy et al. (2011), which is an updated version of the R. C. Kennicutt (1998) nebula line calibration. Those papers assume a continuous (i.e., constant) SFR and solar metallicity. While the SFRs are averaged over 100 Myr, the nebular emission is dominated by light from young massive stars, for continuous star formation, so effectively it only traces the most recent 10 Myr. Using a P. Kroupa (2001) IMF instead makes negligible difference to the calibration (E. J. Murphy et al. 2011). These calibrations ultimately rely on the Starburst 99 stellar models (C. Leitherer et al. 1999).

As a consistency check, we compare the `BAGPIPES` SFR (specifically the instantaneous SFR value, which is effectively close to a 10 Myr averaged value) and Paα SFR. The SFR values have a one-to-one relationship, but the `BAGPIPES` values are on average ∼70% higher, which we put down to the differing stellar population models and different metallicities. We discuss the effect of this difference on our results in Section 4.2.2.

2.2. MIGHTEE 1.23 GHz Continuum Data

The MeerKAT International GHz Tiered Extragalactic Exploration (MIGHTEE; M. Jarvis et al. 2016)[19] survey is a 20 deg^2 survey of well-studied fields to μJy sensitivity conducted by the MeerKAT radio telescope. These observations in GOODS-South were performed in L band covering 856–1711 MHz and are the continuum data from the LADUMA H I survey project (S. Blyth et al. 2016).[20] The processing was performed in a similar manner to I. Heywood et al. (2022) and is described in C. L. Hale et al. (2025).

We use the deep image of the Extended Chandra Deep Field South (ECDFS) from the MIGHTEE Data Release 1 (DR1; C. L. Hale et al. 2025). This image covers 1.5 deg^2, encompassing the GOODS-South region. It was imaged at two different resolutions with restoring beams of 5.5 and 7.″3 FWHM. These images have median measured rms sensitivities at the center of the each field of 1.2 and 1.3 μJy beam^{-1}, respectively. The different resolutions come from using different values of the D. S. Briggs (1995) robust parameter: 0.0 and −1.2 for the low- and high-resolution images, respectively. Also provided is an effective frequency image, which is necessary owing to the size of the MeerKAT primary beam varying across the wide frequency range ($\Delta\nu/\nu\sim1$). The mean effective frequency in the subregion of ECDFS covered by FRESCO is ∼1.23 GHz.

A source catalog is produced by running the `Python Blob Detection and Source Finder` (`PyBDSF`; N. Mohan & D. Rafferty 2015)[21] code on each image. A 3σ threshold is used to detect islands of emission to ensure a high completeness of extended and compact emission, but only 5σ sources were retained in the final catalog. `PyBDSF` also produces rms maps using a sliding box, although the rms may be elevated in certain regions owing to natural source confusion due to the sensitivity of the image. See C. L. Hale et al. (2025) for more details.

We use the 5.″5 image and catalog owing to its superior resolution. This catalog has additionally been cross-matched to host galaxies from the IR using a combined process of both statistical association and visual identification (further details in C. Hale et al. 2026, in preparation). First, each `PyBDSF` source was matched to a K_S-band-selected catalog from the VISTA Deep Extragalactic Observations (VIDEO; M. J. Jarvis et al. 2013) survey. To prepare the K_S-band-selected catalog, a 5σ limiting magnitude of 23.7 was applied and a star/galaxy separation was applied to remove potential stars, using g–i (from the Hyper Suprime Camera Subaru) and J–K_S (from VIDEO) color cuts. A likelihood ratio (LR) technique (see, e.g., W. Sutherland & W. Saunders 1992; K. McAlpine et al. 2013; S. D. Weston et al. 2018; W. L. Williams et al. 2019)

---

[18] We search for Hα observations of our sample, but only one Paα source (in the GOODS-N field; R. E. Skelton et al. 2014) has such data. The nebula attenuation derived from the line ratio is just consistent with that from BAGPIPES (which was also applied to the GOODS-N Paα sample). However, this is just one source with quite high attenuation ($A_V^{\rm neb}({\rm Pa}\alpha{\rm H}\alpha) = 3.1 \pm 0.1$ and $A_V^{\rm neb}({\rm BAGPIES}) = 3.8 \pm 0.7$), so it is difficult to derive substantive conclusions.

[19] https://www.mighteesurvey.org/

[20] https://science.uct.ac.za/laduma

[21] https://pybdsf.readthedocs.io/

was then used to match the radio sources to a host galaxy. A decision tree was then adopted to determine whether the LR was sufficient or visual inspection was required. Reasons for needing visual inspection include, but are not limited to, a source being large such that it might be a lobed AGN and the LR not passing a sufficient threshold (which balanced completeness and reliability). Those sources that needed visual inspection were passed to an internal MIGHTEE Zooniverse (C. Lintott et al. 2012)[22] repository, which provided radio contours and the K_S-band host galaxies overlaid on i (HSC-SSP) and 3.6 μm (from the Spitzer Extragalactic Representative Volume Survey (SERVS); J. C. Mauduit et al. 2012)[23] images. Five people were required to visually classify a source, and a host galaxy was adopted where 60% of these classifications agreed.

2.3. X-Ray Data

We use the deep 7 Ms Chandra X-ray catalog (B. Luo et al. 2017), which covers 484.2 arcmin^{-2} of the ECDFS, including the FRESCO region. This catalog includes 1008 sources that are detected in up to three X-ray bands: 0.5–7.0 keV, 0.5–2.0 keV, and 2–7 keV. In the center of the image sensitivities of 1.9×10^{-17}, 6.4×10^{-18}, and 2.7×10^{-17} erg cm^{-2} s^{-1} are reached in the three bands, respectively.

This 7 Ms catalog is cross-matched with the Paα catalog using a 1″ search radius (as that catalog has positional uncertainties up to 1″). At the sensitivity of this catalog it is possible to probe X-ray luminosities an order of magnitude below the rest-frame X-ray hard-band luminosity threshold for AGN, $L_{2-10\,\mathrm{keV}} > 3 \times 10^{42}$ erg s^{-1}, for the redshift range of this sample ($1.0 \lesssim z \lesssim 1.8$).

2.4. JWST/MIRI Data

Approximately half of the GOODS-S FRESCO survey area is covered by the Systematic Mid-infrared Instrument Legacy Extragalactic Survey (SMILES; G. Rieke et al. 2017). SMILES covers $\sim$34 arcmin^2 (3×5 pointings) with eight bands across $\lambda \sim 5$–27 μm. The 5σ point-source sensitivities range from 0.21 to 15 μJy from the shortest to longest wavelength, significantly deeper than the previous mid-IR data from Spitzer (M. Dickinson et al. 2003; J. C. Mauduit et al. 2012). J. Lyu et al. (2024) use these data in conjunction with the deep NIRCam imaging from the JWST Advanced Deep Extragalactic Survey (JADES; D. J. Eisenstein et al. 2023) to model the SEDs of 3273 mid-IR-detected sources. This SED fitting identified 217 AGN candidates from their warm dust components. Note that our cross-identifications (see Section 3.2.1) include both confirmed AGN in their "massive galaxy" sample (stellar mass $M_* \gtrsim 10^{9.5}\,M_\odot$) and candidate AGN in dwarf galaxies. In the latter case, the differing SEDs of dwarf galaxies, combined with their lower luminosities, makes robust AGN detection via warm dust difficult. In this work, as we want to remove AGN, we take the conservative approach of considering the full sample of candidates as AGN.

2.5. Local Paα Sample

While ground-based observations of local galaxies are complicated by atmospheric absorption, a sample of local ultraluminous or luminous infrared galaxies (U/LIRGs) has been observed using a narrowband (NB) filter at 1.91 μm, which coincides with an atmospheric window (K. Tateuchi et al. 2015). The observations were taken with the Atacama Near Infrared Camera (ANIR; K. Motohara et al. 2008) on the University of Tokyo Atacama Observatory (TAO; Y. Yoshii et al. 2010) 1.0 m telescope (miniTAO; T. Minezaki et al. 2010). The sample of U/LIRGs was selected to be at decl. < -30 deg and to have a small recessional velocity, which would put the Paα line emission in the 1.91 μm NB filter: 2800–8100 km s^{-1} (corresponding to distances of 46.6–109.6 Mpc).

Targets were selected from the Infrared Astronomical Satellite (IRAS) Revised Bright Galaxy Sample (RBGS; D. B. Sanders et al. 2003), and of the 151 RBGS targets matching the decl. and velocity criteria above, 38 RBGS fields were randomly selected for observation. These fields included 44 galaxies in total since 12 galaxies formed six close pairs in the RBGS catalog. The galaxies in the sample were classified by their optical spectra as either H II (star-forming), Seyfert 1/2 (signs of AGN), or LINER (high excitation state potentially associated with AGN activity). We cross-matched this sample with the NRAO VLA Sky Survey (NVSS; J. J. Condon et al. 1998) 1.4 GHz radio catalog using a search radius of 45″ (comparable to the NVSS resolution), finding 32 matches to the 38 fields. The six targets missed are due to the NVSS lower decl. limit of -40 deg.

We use the Paα luminosities reported by K. Tateuchi et al. (2015), as they utilize the same cosmology. For the six close pairs we sum the luminosities, as the relatively low resolution of NVSS can only provide flux densities for the total systems. The total extinction in these systems is determined from the Balmer decrement. K. Tateuchi et al. (2015) then use the D. Calzetti et al. (2000) extinction curve with $R_V = 4.05$ to correct their Paα SFRs for this extinction. We therefore correct their observed Paα luminosities by the ratio of the corrected SFR to the uncorrected SFR. Uncertainties on the final luminosities used here are a combination of the flux uncertainty and the uncertainty on the extinction correction.

3. Analysis

3.1. Cross-matching

We cross-match the Paα catalog with the MIGHTEE radio catalog using the positions of the identified host galaxies of the MIGHTEE radio sources rather than the radio positions. Using a search radius of 0.″5, we find 47 matches. We justify this radius owing to the FRESCO and VIDEO[24] data having positional accuracies of <0.″1 and the galaxies all being <1″ at this redshift. We also cross-match the Paα catalog with the mid-IR SMILE catalog using the same 0.″5 radius. In the left panel of Figure 1 we plot the Paα line luminosities of the full sample as a function of redshift and indicate those sources with MIGHTEE 1.23 GHz detections.

3.2. Identifying AGN

3.2.1. FRESCO z ∼ 1.3 Sample

As this analysis is focused on the radio properties of Paα-selected SFGs, we wish to filter out AGN. Of the 506 FRESCO sources from Section 2.1, 50 are found to have an

---

[22] https://www.zooniverse.org

[23] https://doi.org/10.26131/IRSA407

[24] Which define the host galaxy positions of the MIGHTEE radio sources.

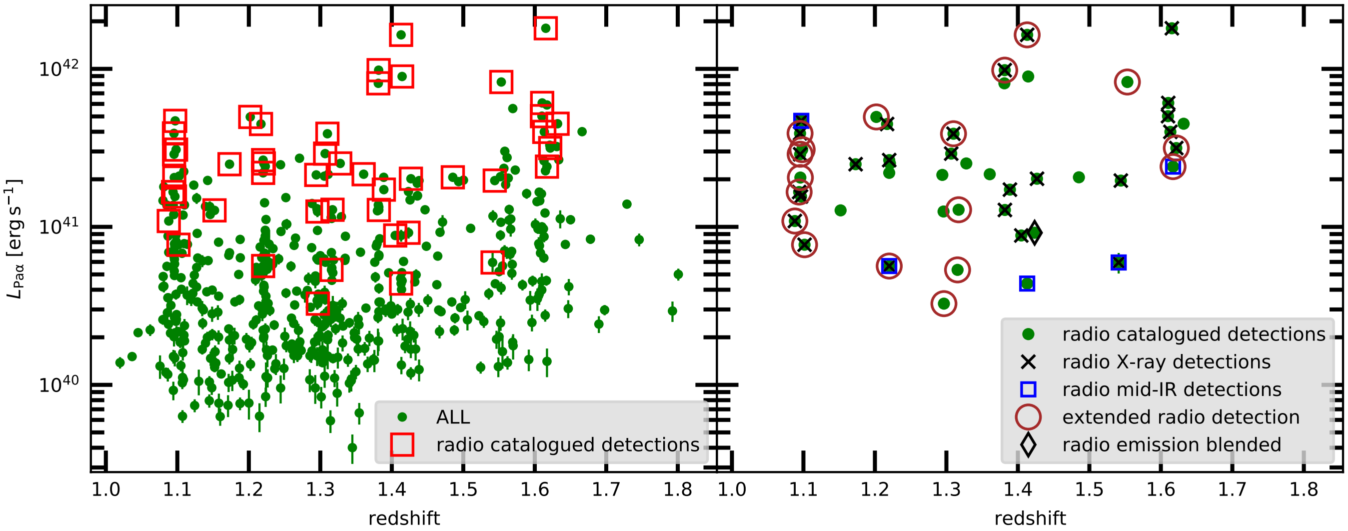

Figure 1. Attenuation-corrected line luminosities with uncertainties plotted against redshift. Left: the 506 Paα sources in the GOODS-South sample, with red squares indicating the 47 sources that match the host galaxies of the cataloged radio sources from the ECDFS MIGHTEE image at 1.23 GHz. Right: radio cataloged detections of Paα sources with AGN identified (as described in Section 3.2). AGN are selected via X-ray detections from a deep Chandra image (B. Luo et al. 2017), from mid-IR warm dust from SED fitting using NIRCam/MIRI data (J. Lyu et al. 2024), or from extended radio emission from MIGHTEE (Section 2.2). One source is removed owing to blended radio emission. Of 47 radio sources, only 11 are SFGs free from AGN activity.

X-ray counterpart, including 26 of the 47 radio detections. While the X-ray luminosities of these sources are below the canonical maximum value used to securely identify AGN ($L_X \geqslant 3 \times 10^{42}$ erg s^{-1}; B. Luo et al. 2017), they are above the luminosity expected for their SFR (e.g., M. Symeonidis et al. 2011), so we conservatively flag them as AGN (although some could be extremely dusty SFGs).

We perform similar removal of AGN using the SMILE catalog of mid-IR-selected AGN. Of the 506 FRESCO sources, 17 are identified as mid-IR AGN, including five sources with radio detections. The SMILE survey only covers around half of the FRESCO survey, so this mid-IR AGN selection is incomplete.

As any SFGs in the final Paα sample are expected to be less than 1″ in size, we can remove extended radio-loud AGN by flagging all radio sources with a nonzero deconvolved size in the image plane. This approach potentially removes some SFGs at low signal-to-noise ratio (SNR), but we would rather lose a few SFGs and minimize the AGN contamination. As the radio resolution of 5.″5 is roughly an order of magnitude larger than the typical sizes of SFGs at this redshift (e.g., A. van der Wel et al. 2014), this selection is a good way to remove radio sources powered by jets and lobes. This selection flags 18 sources. The two Paα sources with broad lines, mentioned in Section 2.1, are both detected in the X-ray and so are excluded by the first step above (one is also a radio detection). We also perform visual inspection to ensure robust cross-matching and remove a further source owing to having another galaxy contribute to the measured radio flux density.

The combined visual/X-ray/mid-IR/radio selections above leave just 11 non-AGN radio detections in the final Paα sample. We indicate the sources identified as AGN in the right panel of Figure 1. Table 1 provides a running count of the Paα sample following these and subsequent selection criteria.

To determine the radio luminosities accurately, we need the spectral indices. As these are unknown, we assume a spectral index (evaluated above 1 GHz) of $\alpha = -0.78 \pm 0.15$, which is the mean and standard deviation of the spectral indices from the local sample of SFGs studied by J. A. Grundy et al. (2025).

Table 1
Breakdown of the 506 Paα Sample Following Cross-matching with the Radio Catalog and Cuts Described in Sections 3.2.1, 3.3, and 3.4

Description	Nondetections	Detections
Full sample	459	47
X-ray AGN	(24)	(26)
Radio AGN	…	(18)
Mid-IR AGN	…	(5)
Visual inspection	…	(1)
Cataloged radio detections	…	11[a]
Blended with radio	(118)	…
Remaining X-ray AGN[b]	(17)	…
Remaining mid-IR AGN[b]	(10)	…
Noncataloged detections	(18)	…
Nondetections	298[c]	…

Notes. Numbers in parentheses represent subsamples to be subtracted from the number above. The final breakdown of non-AGN sources (in bold below) is 11 cataloged radio detections, 18 noncataloged radio detections, and 298 nondetections to be stacked.

[a] The X-ray/radio/mid-IR AGN subsamples overlap, making a total of 35 AGN.

[b] After removing blended sources.

[c] The X-ray and mid-IR AGN subsamples overlap, making a total of 25.

Using a lower spectral index of $\alpha = -0.5$, i.e., with more free–free contribution, only decreases the luminosities by ~20%. To obtain the 1.4 GHz luminosities, we first convert the 1.23 GHz flux densities to 1.4 GHz flux densities, $S_{1.4\mathrm{GHz}}$, using this spectral index. The 1.4 GHz radio luminosity, $L_{1.4\mathrm{GHz}}$, is therefore

$$\frac{L_{1.4\mathrm{GHz}}}{\mathrm{W\ Hz^{-1}}} = 4\pi \left(\frac{d_L}{\mathrm{m}}\right)^2 \frac{S_{1.4\mathrm{GHz}}}{10^{-26}\ \mathrm{Jy}} (1+z)^{-1-\alpha}, \tag{2}$$

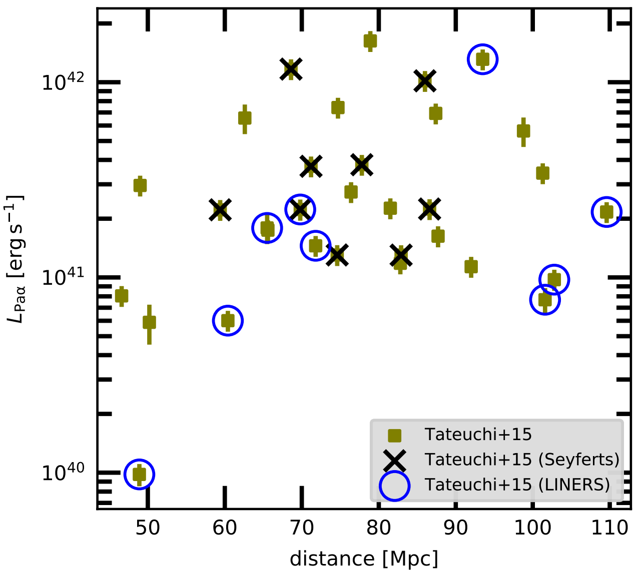

Figure 2. Distribution in Paα luminosity/distance parameter space of the local sample from K. Tateuchi et al. (2015) as presented in Section 2.5. Sources with Seyfert or LINER indicators in their optical spectrum are marked. These are removed from further analysis to avoid contamination by AGN as discussed in Section 3.2.2.

where d_L is the luminosity distance at a redshift z and $S_{1.4\mathrm{GHz}}$ is the 1.4 GHz observed-frame flux density. The uncertainties on the radio luminosities are propagated from the flux and spectral index uncertainties, as we assume that all redshifts have negligible uncertainties.

3.2.2. Local $z < 0.1$ Sample

From visual inspection, the radio emission of all the local sources appears to be related to star formation, i.e., no signs of jets or lobes are apparent, with the emission broadly tracing the underlying optical images. The spectral classification provided by K. Tateuchi et al. (2015) allows us to identify potential AGN in the local sample. We remove sources clearly identified as AGN from a Seyfert classification (nine sources) and, out of an abundance of caution, also remove those with a LINER classification (nine sources), as the high excitation state of LINERs could be due to an AGN. Hence, in Figure 2 we plot the Paα luminosities as a function of distance of the local sample, indicating which sources are classified as Seyfert galaxies or LINERs. In subsequent analysis we remove these two AGN subsets, leaving just 14/32 local sources. Radio luminosities are determined via Equation (2), but note that the k-correction is negligible at very low redshift.

3.3. FRESCO Paα Sources Blended with Radio

The lower resolution of the radio image, by about an order of magnitude, compared to the typical size of SFGs found by the Paα detections at this redshift presents a challenge for the stacking. We do not want to stack Paα sources that have nearby but unrelated radio emission; hence, we remove all non-radio-detected Paα sources that lie within $7''$ of a cataloged radio source. We find that we have to use a $7''$ radius, larger than the FWHM of the radio image ($5''.5$), in order to be sure that none of the remaining nondetected Paα sources have radio flux densities contaminated by nearby sources. This cut finds a total of 118 potentially blended sources (including three from visual inspection). The blended Paα sources include seven with X-ray detections, so the number of Paα sources without radio detections, but with X-ray detections, falls to 17.

3.4. Stacking of FRESCO Paα Sources

To obtain the mean radio flux density of the Paα sources without radio detections, we can stack in the radio image. Given the $5''.5$ resolution of MIGHTEE, all the FRESCO Paα SFGs will be unresolved, so the flux from a single pixel provides a good measure of the total flux.

3.4.1. Background Subtraction and Confusion Noise

When stacking at the positions of the Paα sources, we have to subtract the background in the radio image. We take all the pixels in the FRESCO subregion of the ECDFS MIGHTEE image and fit a Gaussian to just the negative side of a histogram of their values. We then equate the background to being the mean of this Gaussian. From this method we obtain a local background of $-0.97\,\mu$Jy, which we subtract from the flux density at each pixel.

We also have to account for confusion noise since the radio images are approaching the confusion limit. To determine the amount of flux contributing to each pixel from nearby nonassociated radio sources, we take 10,000 realizations of 298 random positions (i.e the same number we stack later) and measure the median flux each time. We then take the mean of these 10,000 medians to estimate the confusion noise to be subtracted. From this method we obtain a confusion noise of $0.46 \pm 0.17\,\mu$Jy beam^{-1}, with the uncertainty being the standard deviation of the 10,000 realizations.

So for the corrected single pixel flux measurements we subtract our estimates of both the background in the FRESCO region and the confusion noise. We note that this method accounts for the confusion noise statistically rather than on an individual basis, but it is appropriate given the sample size and depth.

3.4.2. Noncataloged Detections

Using the local rms image, we can determine the SNR of these sources without counterparts in the radio catalog using the corrected flux measurement described above. We plot the distribution of the SNR in Figure 3 and find a tail of sources with positive SNRs that extends to 5σ, but with one source at 6.0σ. Above 3σ we find 18 sources that we do not stack but treat as “noncataloged radio detections.” We determined their radio luminosities and uncertainties in the same manner as the cataloged radio detections.

The sole $>5\sigma$ detection is likely due to the complication of using a source finder on a crowded, confusion-limited survey where estimating the local rms is complex. Visual inspection suggests that this is real radio flux likely associated with the Paα emitter missed by `PyBDSF`. Hence, we include the 6.0σ noncataloged radio detection going forward, but its inclusion does not materially affect the results.

3.4.3. Paα Sources Blended with Each Other

The low resolution of the MIGHTEE radio data also means that some of these nondetections and noncataloged detections will be close enough together to be within the same resolution

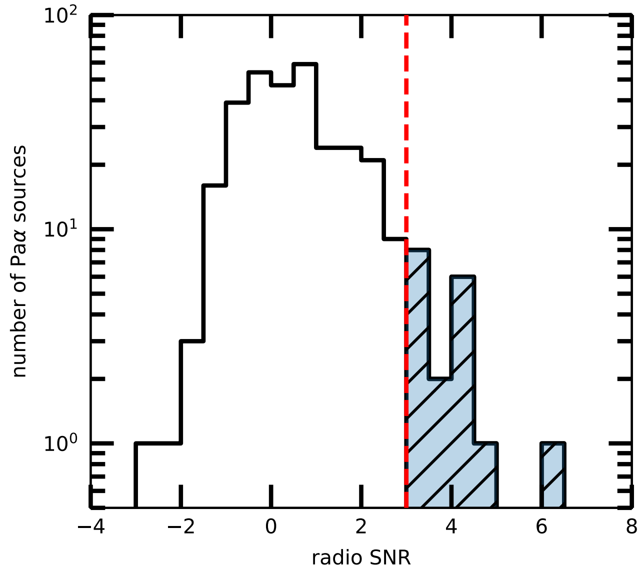

Figure 3. Histogram of the SNR of MIGHTEE flux density pixel values at the positions of Paα sources without counterparts in the radio catalog. The 18 sources with values above 3σ (vertical dashed line) are considered noncataloged detections.

element of the radio image. We check for close pairs using a 5.″5 radius and find 3 and 64 close pairs from the 18 noncataloged detections and the 298 remaining nondetections, respectively. In all cases, these pairs are far enough apart that they have different radio flux densities from separate, albeit very close, pixels. However, these nearby pixel-based radio fluxes are not independent measurements when there are two Paα sources within one radio resolution element.

We make the assumption that the two Paα sources both contribute to the radio flux and that the total radio flux is the higher of the two pixel values. Hence, we take the higher flux density value and assign a portion of the radio emission to each of the pair based on their relative Paα flux (from the assumption that the two values are indeed correlated).[25] For the stacked sample this is equivalent to assigning the higher flux density to just one source. Sharing the flux by the Paα flux ratio affects 6 of the 18 noncataloged radio detections by decreasing their radio luminosity.

3.4.4. Stacking Method

The final stacked flux density is simply the median of the MIGHTEE pixel values, corrected for background and confusion noise, at the positions of each of the 298 Paα sources (including the cases where we reevaluated the flux densities of close pairs of sources). We find a median value of 0.56 μJy, which is a little lower than the mean, 0.59 μJy. The mean being close to the median suggests that there is not a significant bright tail of sources (potentially radio-excess AGN) left in the stack.

To estimate the uncertainty on this stacked flux, we repeat the stacking process at 298 random positions 10,000 times. We then take the standard deviation of these 10,000 trials as the uncertainty on the stacked flux density, 0.18 μJy, which provides a 3.3σ stacked flux density value.

The radio luminosity of the stack is determined from the stacked flux using Equation (2) and the mean redshift of the 298 sources ($\langle z\rangle = 1.31$). We obtain a radio luminosity of $L_{1.4\mathrm{GHz}} = (5.5 \pm 1.9) \times 10^{21}$ W Hz^{-1}, where the uncertainty is the propagated combination of the flux uncertainty and that of the spectral index. We note that we could have determined the radio luminosity of each of the 298 nondetections separately (using the individual pixel flux densities) and then taken the mean. Doing so, in fact, gives a very similar value: $L_{1.4\mathrm{GHz}} = 5.6 \times 10^{21}$ W Hz^{-1}.

3.5. Modeling

3.5.1. Calibrating the Radio/SFR Conversion at z ∼ 1.3

From our final FRESCO sample of AGN-free SFGs (11 cataloged radio detections, 18 noncataloged radio detections, and the 298 nondetections) we have an opportunity to investigate the radio luminosity/SFR correlation for a well-defined sample with well-determined SFRs at $z \sim 1.3$. We use the Python routine `linmix` (B. C. Kelly 2007), which uses a hierarchical Bayesian approach to linear regression. This code accounts for uncertainties on the both the x- and y-axes as well as nondetections in the y-axis (as we have here). `linmix` runs a Markov Chain Monte Carlo, randomly sampling from the posterior, to produce samples from the posterior distribution of the model parameters, given the data. The `linmix` algorithm is based on a model that derives a likelihood function for the measured data and assumes that the distribution of two variables can be approximated using a mixture of Gaussians. In the case of nondetections or limits, the likelihood function is modified to include this selection effect. We fit the data in log-space so that the linear relation provides a power law. For the undetected sources we use their 3σ flux densities as upper limits.

3.5.2. Modeling High (and Low) Radio Luminosities

Figure 4 shows a number of SFGs with relatively high radio luminosities for their SFR, i.e., very low TFs $\leqslant$5%. We investigate whether at least some of the scatter of sources around these correlations could be due to the radio luminosity being a delayed probe of star formation. Recent work (R. H. W. Cook et al. 2024) suggests that radio emission in SFGs correlates better with the SFR a few hundred Myr in the past (as inferred from SFHs derived from SED modeling) than with tracers of the current SFR.

The relativistic electrons, cosmic rays (CRs), responsible for the synchrotron emission are produced at the end of the lives of the most massive stars, which can live for 10–30 Myr for Type II supernova progenitors. The timescale of the synchrotron emission depends on the lifetime of the CRs, and there is growing evidence that the radio emission is a delayed tracer of SFR by potentially up to a few hundred Myr as suggested by R. H. W. Cook et al. (2024). Estimates of the total lifetime of these CRs vary, as there are two contributions: the synchrotron cooling time and the escape time from the galaxy. The former has estimates of 10–100 Myr (V. Heesen et al. 2023), and the latter can be 20–300 Myr (J. Dörner et al. 2023). Combining these results gives total lifetimes ranging across 7–75 Myr.

Tracers of the SFR that come directly from the interstellar medium in star-forming regions include the free–free radio emission and the hydrogen recombination lines such as Paα.

---

[25] Note that assigning this radio flux equally to the two sources in a pair does not substantially affect the results.

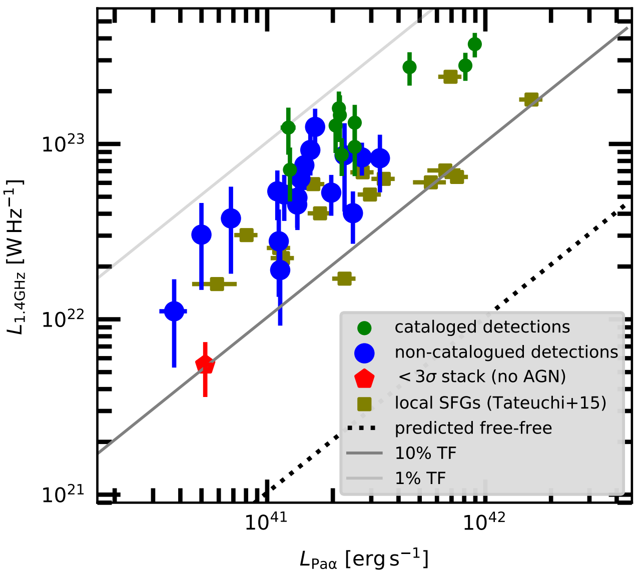

Figure 4. Radio luminosity plotted as a function of Paα luminosity for our various AGN removed subsamples: the 11 cataloged radio detections, the 18 noncataloged detections, and the stack of the 298 remaining nondetections after removing blended sources. The local sample of 14 Paα emitters from K. Tateuchi et al. (2015), minus AGN, is also plotted. Both axes have error bars plotted, which are sometimes smaller than the symbol. Overlaid as lines are the expected 1.4 GHz free–free luminosity from a Paα source, as well as ×10 and ×100 this value, which corresponds to 10% and 1% 1.4 GHz TFs, respectively. Nearly all galaxies have TFs in the range 1%–10%, with the local sample having slightly higher TF.

These are expected to be nearly instantaneous (delayed by just 10 Myr and averaged over the past 10 Myr).

Here we create a toy model where we follow the recent SFR (as traced by Paα) and the total radio emission (free–free plus synchrotron emission) through a starburst phase, but with the synchrotron emission delayed by 20 Myr (the mean time for the massive stars to go supernova) and then averaged over the previous 75 Myr, the upper limit of the potential range. The delay and average timescales for all components are summarized in Table 2.

In order to follow our toy model during an increasing and decreasing starburst phase, we use a Cauchy–Lorentz function for the SFH, as it has an approximate exponential rise and fall timescale. This model has a base SFR of 3 $M_{\odot}$ yr^{-1} and a peak SFR of 30 $M_{\odot}$ yr^{-1}, with a timescale (γ in the Cauchy–Lorentz function) of 100 Myr. The relative SFRs are chosen to represent the likely extremes of starbursting and quenching, but the absolute values are arbitrary and chosen to fit within the distribution of observed Paα sources. While rapid changes are uncommon in the local Universe, they may not be at high redshift as seen in hydrodynamical simulations (e.g., A. L. Muratov et al. 2015), although the timescale here, 100 Myr, is quite rapid. We discuss how these choices affect the results in Section 4.2.2. From this model we trace the instantaneous SFR and the delayed radio emission over time.

As the radio emission is a combination of synchrotron and free–free, we assume an initial TF of 5% at 1.4 GHz (TF$_{1.4}$ as typically seen in local starbursts; T. J. Galvin et al. 2018; J. A. Grundy et al. 2025). We can trace the evolution of the observed TF$_{1.4}$. We use the SFR-to-radio-luminosity conversion factor determined in the previous section to convert the delayed SFR into a radio luminosity. However, our choice of conversion factor is not important, as this only normalizes the evolutionary tracks and we are interested in the deviation from the mean value.

Table 2
Timescales for the Delay (Relative to the Star Formation) and for the Average over the Prior Period for the Toy Starburst Model

Component	Timescale	Duration
Paα	delay	10 Myr
	average	10 Myr
Free–free	delay	10 Myr
	average	10 Myr
Synchrotron	delay	20 Myr
	average	75 Myr

4. Results and Discussion

4.1. Radio v Paα Luminosities

In Figure 4 we plot the radio luminosity against the Paα luminosity of the detected radio sources, the noncataloged radio detections, the local sample, and the stacked value. The cataloged sources are naturally above the noncataloged radio detections, which in turn are above the stacked limit. This distribution is clearly due to the sensitivity of the radio survey, which applies a roughly constant luminosity cut for this redshift range. The stacked value clearly accounts for the radio luminosities of the nondetected radio sources, which undoubtedly extend down to 10^{21} W Hz^{-1} and below.

In Figure 4 we also present the predicted free–free 1.4 GHz luminosity for a given Paα luminosity using

$$\frac{L_{\mathrm{ff}}(\nu)}{\mathrm{W\,Hz^{-1}}} = 1.062\,\times\,10^{-20}\left(\frac{T}{10^{4}\,\mathrm{K}}\right)^{0.45} \times\left(\frac{\nu}{\mathrm{GHz}}\right)^{-0.1}\frac{L_{\mathrm{Pa}\alpha}}{\mathrm{erg\ s^{-1}}}, \tag{3}$$

where $L_{\mathrm{ff}}(\nu)$ is the free–free luminosity as a function of frequency and T is the temperature of the ISM (which we take to be 10^4 K as before). This equation comes from combining the relationship of the photoionization rate and thermal radio luminosity (R. H. Rubin 1968) and that between the photoionization rate and Paα luminosity (R. C. Kennicutt 1998). Combining this equation with Equation (1) gives a result within 10% of other free–free/SFR relations used in the literature (e.g., E. J. Murphy et al. 2011, who used a different IMF).

It is interesting to note the range of TFs of this sample at 1.4 GHz, TF$_{1.4\mathrm{GHz}}$. Generally for low-z SFGs the TF$_{1.4\mathrm{GHz}}$ varies from around 1% to 10%–30% in some extreme cases (T. J. Galvin et al. 2018; J. A. Grundy et al. 2025). The local sample has TF$_{1.4\mathrm{GHz}} \approx 2\%$–20%, whereas the $z \sim 1.3$ detected Paα sample (cataloged and noncataloged) ranges from $\approx$1% to 10%. We note that the lack of high TF$_{1.4\mathrm{GHz}}$ in the detected sample is due to selection effects, i.e., we are biased against directly detecting sources with low radio luminosities for their Paα luminosity. We investigate whether the low-TF$_{1.4\mathrm{GHz}}$ sources are fading starbursts where the radio emission is still high owing to the delayed timescales of synchrotron emission using the model described in Section 3.5.2. We show these models in Figure 5 and discuss them in Section 4.2.2.

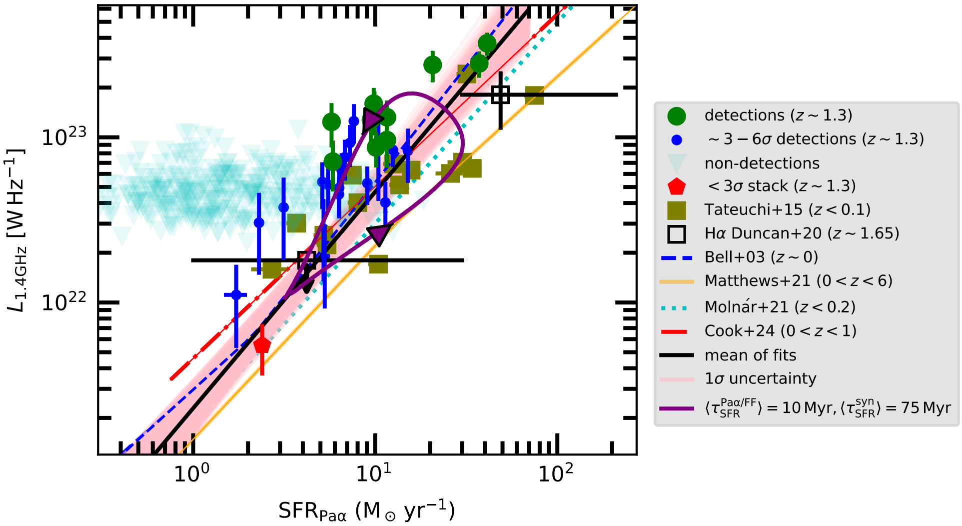

Figure 5. Radio luminosity plotted as a function of Paα SFR for our various subsamples after the removal of AGN: the 11 cataloged radio detections, the 18 noncataloged radio detections, the 14 local sources, and the 298 remaining Paα nondetections. We also present the stacked value of these nondetections, although it is not used in the fitting. For comparison we present the Hα/radio luminosity results from K. J. Duncan et al. (2020) at $z \sim 1.65$. We overlay various conversion factors from the literature, including E. F. Bell (2003), D. C. Molnár et al. (2021), R. H. W. Cook et al. (2024), and A. M. Matthews et al. (2021), as well as indicating the redshift range they were evaluated over (the length of the line indicates the SFR range they were determined over). The best-fit radio luminosity/SFR correlation is presented (see Section 3.5.1), with the pink tracks representing solutions within 1σ of the median fit of both parameters. We also overlay a starburst evolutionary track as described in Section 3.5.2, with the arrows indicating the direction of time. The starburst has a Cauchy–Lorentz (pseudo-exponential) rise and fall temporal form, with the synchrotron component of the radio luminosity delayed by 20 Myr (compared to 10 Myr for the Paα and free–free components). The SFRs are averaged over the previous 10 and 75 Myr for the Paα SFR/free–free luminosity and synchrotron luminosity, respectively. This model can partly explain the scatter around the best-fit line in this and other works.

4.2. Radio Luminosity versus SFR

In Figure 5 we plot the radio luminosity against the Paα-derived SFR, overlaid with four different 1.4 GHz luminosity-to-SFR conversion factors (E. F. Bell 2003; A. M. Matthews et al. 2021; D. C. Molnár et al. 2021; R. H. W. Cook et al. 2024; all with a Chabrier IMF). While there are many more relations in the literature, these four are chosen to demonstrate the breadth of relations in use. Each is determined over a different redshift range as indicated in the legend. If one includes the stacked data point representing 298 SFGs, we can see that the data here are consistent with these different relations, albeit with a scatter at high radio luminosities, which we discuss in Section 4.2.2. The local sample also agrees well with these previous relations.

4.2.1. Correlation and Fit

The result of the power-law fit (using `linmix`) to the data at $z \sim 1.3$ is

$$L_{1.4\mathrm{GHz}}[\mathrm{W\,Hz^{-1}}] = 10^{21.36\pm0.17} \times \mathrm{SFR}_{\mathrm{Pa}\alpha} \times [M_\odot\ \mathrm{yr}^{-1}]^{1.31\pm0.17}, \tag{4}$$

where the values are the medians and the uncertainties are the 68.2 (1σ) percentile limits. We plot this fit in Figure 5. For reference we overlay all chain models from the `linmix` fitting that have parameter values within 1σ of the best-fit values as indicated by the pink region.

This fit is consistent with most of the previous relations plotted (e.g., E. F. Bell 2003; D. C. Molnár et al. 2021; R. H. W. Cook et al. 2024), demonstrating that this Paα-selected sample follows other commonly derived 1.4 GHz luminosity-to-SFR conversions. We note that our relation and others lie around 0.5 dex above the A. M. Matthews et al. (2021, hereafter M21) relation at the high-SFR end (i.e., 50–100 $M_\odot$ yr^{-1}). The M21 result comes from a fit to the source counts and a $P(D)$ analysis down to $\sim$0.2 μJy, so it is probing the brightest radio sources across all redshifts. Hence, part of the fit comes from the luminous SFG at $z > 3$, where IC losses may become important (e.g., I. H. Whittam et al. 2024). The radio luminosity/SFR conversion from M21 does not account for a potential variation in redshift, so we postulate that the difference seen in Figure 5 could be due to unaccounted-for IC losses. Direct calibration of the radio luminosity/SFR conversion at $z > 3$ would confirm this or not.

Our result also agrees well with observational data at $z \sim 1.65$ from K. J. Duncan et al. (2020), although their high SFR datum is marginally lower. The fit also broadly agrees with the local sample. In order to improve our fit, we would need some combination of more direct detections, a larger sample, and probing higher and lower SFRs. We note that our result is not driven by systematics, for example, changes to the dust attenuation or the radio k-corrections only shift luminosities by up to 0.1–0.2 dex. In addition, if we increase the confusion noise from 0.45 to 0.8 μJy beam^{-1}, a few sources switch from noncataloged detections to nondetections, but the overall fit remains the same to one decimal place.

4.2.2. High/Low Radio Luminosities

As described in Section 3.5.2, we have developed a toy model to explain the SFGs with relatively high or low radio luminosities for their SFRs/Paα luminosities. This model assumes that the dominant synchrotron emission is delayed by 10 Myr relative to the Paα and free–free emission and that the Paα/free–free emission and synchrotron emission are averaged over 10 and 75 Myr, respectively. We present this evolutionary track in Figure 5.

The track initially increases more rapidly in SFR$_{\mathrm{Pa}\alpha}$ than $L_{1.4\mathrm{GHz}}$, with the SFR$_{\mathrm{Pa}\alpha}$ peaking and then starting to decline before the $L_{1.4\mathrm{GHz}}$ peaks. The $L_{1.4\mathrm{GHz}}$ then peaks before declining more rapidly than $\mathrm{SFR}_{\mathrm{Pa}\alpha}$ for the track to end up at the start. The model shows that a delay in the synchrotron emission can cause a scatter of almost 1 dex, covering a large part of the range of sources lying on this correlation. Due to the radio detection limit, we do not directly sample the full range of scatter below the fitted relation for the Paα sample. Using a shorter or longer delay or time average would cause a narrower or wider scatter, respectively, although we note that the width of the scatter is driven more by the time averaging unless the delay time becomes comparable to the average time. This toy delayed/averaged synchrotron model can potentially explain some of the scatter observed in the radio luminosity/Paα SFR relation and indeed any relation between radio luminosity and a more instantaneous measure of SFR (e.g., the radio/far-IR relation).

We caution the reader that there may be other effects, on top of measurement error, that could contribute to the scatter. Uncertainty in the dust correction for the Paα sources leads to shifts of ∼0.1 dex. The choice of the IMF has a negligible effect on the Paα-derived SFR (E. J. Murphy et al. 2011), although the ionizing spectrum hardness may have a stronger effect. Other factors affect the $\mathrm{SFR}_{\mathrm{Pa}\alpha}$ estimate, including the underlying choice of stellar populations and metallicity. As an example, the ∼70% offset with the `BAGPIPES` SFR shows that systematic shifts can occur. However, systematic shifts simply change the normalization in Figure 5. The radio emission also depends on the total magnetic field of the galaxy; however, this is found to vary by only a factor of a few (F. S. Tabatabaei et al. 2017; F. Tabatabaei et al. 2025). It is hard to see how effects like varying geometries and uneven dust distribution can substantially add to the scatter. Potentially changes to the synchrotron spectrum from synchrotron or ionization losses could contribute, but this is expected to only become dominant at very high redshifts ($z > 3$; I. H. Whittam et al. 2025).

While the underlying TF may also be a source of systematic uncertainty, this model can also explain the wide range of TFs observed in local galaxies (e.g., T. J. Galvin et al. 2018; S. Dey et al. 2022, 2024) since the free–free contribution rises and falls before the synchrotron component. The TF reaches a minimum of ∼1% and a maximum of ∼20% at the farthest distances away from the best-fit relation. Hence, the TF could act as a tracer of the age of a starburst in extreme situations, e.g., the very high TF seen in Haro 11 (L. Komarova et al. 2024; J. A. Grundy et al. 2026, in preparation).

A prediction of this model is that young starbursts with rising SFRs would lie below the correlation, have higher TFs, and have flatter spectral indices. Old starbursts with declining SFRs, on the other hand, would lie above the correlation, with low TF and steeper spectra. Upcoming MIGHTEE S-band (2–4 GHz) data may potentially be able to test the variation in spectral index above/below the radio/SFR. Furthermore, in such a scenario, outliers above/below the radio/SFR relation would feature distinct star formation change parameters (E. Wang & S. J. Lilly 2020). These predictions will be investigated in future work.

5. Conclusions

We have investigated the radio properties of a sample of JWST/FRESCO Paα-selected sources across $1 \lesssim z \lesssim 1.8$ in order to determine whether the SFGs at this epoch follow previously derived radio-luminosity-to-SFR conversions. Our main results are as follows:

1. Of 506 FRESCO Paα sources in the GOODS-South, 47 match with the hosts of cataloged radio sources at 1.23 GHz from the MIGHTEE ECDFS image.
2. Removing likely AGN and blended sources leaves a sample of SFGs composed of 11 cataloged radio detections, 18 noncataloged radio detections, and 298 undetected sources.
3. Stacking the undetected sources in flux space, we obtain a 3.3σ detection.
4. The full FRESCO Paα sample spans approximately two orders of magnitude in both Paα and radio luminosity. Overlaying this sample, along with a local sample of Paα SFGs, we find that they follow existing correlations of radio luminosity and SFR across a range of redshifts from the literature.
5. Specifically, by fitting our $z \sim 1.3$ sources (cataloged detections, noncataloged detections, and nondetections), we find a relation of $\log(L_{1.4\mathrm{GHz}}) = (1.31 \pm 0.17) \times \log(\mathrm{SFR}_{\mathrm{Pa}\alpha}) + (21.36 \pm 0.17)$, which is consistent with the literature values.
6. Some of the width of the scatter in the $L_{1.4\mathrm{GHz}}/\mathrm{SFR}_{\mathrm{Pa}\alpha}$ correlation can be explained by synchrotron emission being a delayed/averaged tracer of star formation by 10/75 Myr.

We have confirmed that this sample of SFGs does have radio luminosities consistent with previous calibrations of the $L_{1.4\mathrm{GHz}}$/SFR relation. We can explain some of the scatter in this relation as well, but more sophisticated models with more realistic SFHs are needed to elaborate on the toy model presented here, as well as more direct detections of high-z SFGs in the radio. However, we have demonstrated that this concept is a feasible explanation for a good part of the scatter. Furthermore, this model provides predictions for the nature of the radio emission for rising and declining starbursts that can be tested in the future.

Acknowledgments

We acknowledge the Noongar people as the traditional owners and custodians of Whadjuk Boodjar, the land on which the majority of this work was completed. We thank the reviewer for their careful reading and constructive comments.

N.S. thanks Anshu Gupta and Arash Bahramian for useful discussions. C.L.H., I.H.W., and M.J. acknowledge support from the Oxford Hintze Centre for Astrophysical Surveys, which is funded through generous support from the Hintze Family Charitable Foundation. C.L.H. also acknowledges support from the Science and Technology Facilities Council (STFC) through grant ST/Y000951/1. R.A.M. acknowledges support from the Swiss National Foundation (SNSF) through project grant 200020_207349. I.S. acknowledges funding from the European Research Council (ERC) DistantDust (grant No. 101117541) and the Atraccíon de Talento grant No. 2022-T1/TIC-20472 of the Comunidad de Madrid, Spain. This research was supported by an Australian Government Research Training Program (RTP) Scholarship doi:10.82133/C42F-K220. R.B. acknowledges support from an STFC Ernest Rutherford Fellowship (grant No. ST/T003596/1)

This work is based in part on observations made with the NASA/ESA/CSA James Webb Space Telescope. The data were obtained from the Mikulski Archive for Space Telescopes at the Space Telescope Science Institute, which is operated by the Association of Universities for Research in Astronomy, Inc., under NASA contract NAS 5-03127 for JWST. These observations are associated with program #1895.

The MeerKAT telescope is operated by the South African Radio Astronomy Observatory, which is a facility of the National Research Foundation, an agency of the Department of Science and Innovation. We acknowledge the use of the ilifu cloud computing facility (https://www.ilifu.ac.za/), a partnership between the University of Cape Town, the University of the Western Cape, Stellenbosch University, Sol Plaatje University, and the Cape Peninsula University of Technology. The Ilifu facility is supported by contributions from the Inter-University Institute for Data Intensive Astronomy (IDIA)—a partnership between the University of Cape Town, the University of Pretoria and the University of the Western Cape, the Computational Biology division at UCT, and the Data Intensive Research Initiative of South Africa (DIRISA). The authors acknowledge the Centre for High Performance Computing (CHPC), South Africa, for providing computational resources to this research project.

Based on data products from observations made with ESO Telescopes at the La Silla Paranal Observatory under ESO program ID 179.A-2006 and on data products produced by the Cambridge Astronomy Survey Unit on behalf of the VIDEO consortium.

The Hyper Suprime-Cam (HSC) collaboration includes the astronomical communities of Japan and Taiwan and Princeton University. The HSC instrumentation and software were developed by the National Astronomical Observatory of Japan (NAOJ), the Kavli Institute for the Physics and Mathematics of the Universe (Kavli IPMU), the University of Tokyo, the High Energy Accelerator Research Organization (KEK), the Academia Sinica Institute for Astronomy and Astrophysics in Taiwan (ASIAA), and Princeton University. Funding was contributed by the FIRST program from the Japanese Cabinet Office; the Ministry of Education, Culture, Sports, Science and Technology (MEXT); the Japan Society for the Promotion of Science (JSPS); Japan Science and Technology Agency (JST); the Toray Science Foundation; NAOJ; Kavli IPMU; KEK; ASIAA; and Princeton University.

This paper makes use of software developed for Vera C. Rubin Observatory. We thank the Rubin Observatory for making their code available as free software at http://pipelines.lsst.io/.

This paper is based on data collected at the Subaru Telescope and retrieved from the HSC data archive system, which is operated by the Subaru Telescope and Astronomy Data Center (ADC) at NAOJ. Data analysis was in part carried out with the cooperation of Center for Computational Astrophysics (CfCA), NAOJ. We are honored and grateful for the opportunity of observing the Universe from Maunakea, which has the cultural, historical, and natural significance in Hawaii.

Facilities: JWST (NIRSpec), MeerKAT.

Software: astropy (Astropy Collaboration et al. 2013, 2018).

ORCID iDs

Nick Seymour https://orcid.org/0000-0003-3506-5536
Catherine Hale https://orcid.org/0000-0001-6279-4772
Imogen Whittam https://orcid.org/0000-0003-2265-5983
Pascal Oesch https://orcid.org/0000-0001-5851-6649
Alba Covelo-Paz https://orcid.org/0000-0002-9672-3005
Stijn Wuyts https://orcid.org/0000-0003-3735-1931
J. Afonso https://orcid.org/0000-0002-9149-2973
R. A. A. Bowler https://orcid.org/0000-0003-3917-1678
Joe Arthur Grundy https://orcid.org/0000-0002-4440-8046
Ravi Jaiswar https://orcid.org/0000-0003-2035-3850
Matt Jarvis https://orcid.org/0000-0001-7039-9078
Allison Matthews https://orcid.org/0000-0002-6479-6242
Romain A. Meyer https://orcid.org/0000-0001-5492-4522
Chloe Neufeld https://orcid.org/0000-0002-6558-9894
Naveen A. Reddy https://orcid.org/0000-0001-9687-4973
Irene Shivaei https://orcid.org/0000-0003-4702-7561
Dan Smith https://orcid.org/0000-0001-9708-253X
Rohan Varadaraj https://orcid.org/0009-0006-9953-6471
Michael A. Wozniak https://orcid.org/0000-0002-1033-3656
Lyla Jung https://orcid.org/0000-0001-5512-3735

References

Algera, H. S. B., van der Vlugt, D., Hodge, J. A., et al. 2020, ApJ, 903, 139
Alonso-Herrero, A., Rieke, G. H., Rieke, M. J., et al. 2006, ApJ, 650, 835
Arnaudova, M. I., Smith, D. J. B., Hardcastle, M. J., et al. 2025, MNRAS, 542, 2245
Astropy Collaboration, Price-Whelan, A. M., Sipőcz, B. M., et al. 2018, AJ, 156, 123
Astropy Collaboration, Robitaille, T. P., Tollerud, E. J., et al. 2013, A&A, 558, A33
Bell, E. F. 2003, ApJ, 586, 794
Blyth, S., Baker, A. J., Holwerda, B., et al. 2016, in MeerKAT Science: On the Pathway to the SKA (SISSA), 4
Bonato, M., Prandoni, I., De Zotti, G., et al. 2021, A&A, 656, A48
Briggs, D. S. 1995, PhD thesis, New Mexico Inst. Mining and Technology
Bruzual, G., & Charlot, S. 2003, MNRAS, 344, 1000
Calzetti, D. 1997, AJ, 113, 162
Calzetti, D., Armus, L., Bohlin, R. C., et al. 2000, ApJ, 533, 682
Carnall, A. C., McLure, R. J., Dunlop, J. S., & Davé, R. 2018, MNRAS, 480, 4379
Chabrier, G. 2003, PASP, 115, 763
Clemens, M. S., Scaife, A., Vega, O., & Bressan, A. 2010, MNRAS, 405, 887
Cochrane, R. K., Kondapally, R., Best, P. N., et al. 2023, MNRAS, 523, 6082
Condon, J. J. 1992, ARA&A, 30, 575
Condon, J. J., Anderson, M. L., & Helou, G. 1991, ApJ, 376, 95
Condon, J. J., Cotton, W. D., Greisen, E. W., et al. 1998, AJ, 115, 1693
Cook, R. H. W., Davies, L. J. M., Rhee, J., et al. 2024, MNRAS, 531, 708
Covelo-Paz, A., Giovinazzo, E., Oesch, P. A., et al. 2025, A&A, 694, A178
Delhaize, J., Smolčić, V., Delvecchio, I., et al. 2017, A&A, 602, A4
Delvecchio, I., Daddi, E., Sargent, M. T., et al. 2021, A&A, 647, A123
Dey, S., Goyal, A., Małek, K., & Díaz-Santos, T. 2024, ApJ, 966, 61
Dey, S., Goyal, A., Małek, K., et al. 2022, ApJ, 938, 152
Dickinson, M., Giavalisco, M. & GOODS Team 2003, in The Mass of Galaxies at Low and High Redshift, ed. R. Bender & A. Renzini (Springer), 324
Dörner, J., Reichherzer, P., Becker Tjus, J., & Heesen, V. 2023, A&A, 669, A111
Duncan, K. J., Shivaei, I., Shapley, A. E., et al. 2020, MNRAS, 498, 3648
Eisenstein, D. J., Willott, C., Alberts, S., et al. 2023, arXiv:2306.02465
Falcke, H., Rieke, M. J., Rieke, G. H., Simpson, C., & Wilson, A. S. 1998, ApJL, 494, L155
Galvin, T. J., Seymour, N., Marvil, J., et al. 2018, MNRAS, 474, 779
Grundy, J. A., Seymour, N., Wong, O. I., et al. 2025, PASA, 42, e002
Hale, C. L., Heywood, I., Jarvis, M. J., et al. 2025, MNRAS, 536, 2187
Harwit, M., & Pacini, F. 1975, ApJL, 200, L127
Heesen, V., de Gasperin, F., Schulz, S., et al. 2023, A&A, 672, A21
Heywood, I., Jarvis, M. J., Hale, C. L., et al. 2022, MNRAS, 509, 2150

Hill, G. J., Goodrich, R. W., & Depoy, D. L. 1996, ApJ, 462, 163
Hummel, E. 1991, A&A, 251, 442
Ivison, R. J., Magnelli, B., Ibar, E., et al. 2010, A&A, 518, L31
Jarvis, M., Seymour, N., Afonso, J., et al. 2015, in Advancing Astrophysics with the Square Kilometre Array (AASKA14) (SISSA), 68
Jarvis, M., Taylor, R., Agudo, I., et al. 2016, in MeerKAT Science: On the Pathway to the SKA (SISSA), 6
Jarvis, M. J., Bonfield, D. G., Bruce, V. A., et al. 2013, MNRAS, 428, 1281
Kelly, B. C. 2007, ApJ, 665, 1489
Kennicutt, R. C., & Evans, N. J. 2012, ARA&A, 50, 531
Kennicutt, R. C., Jr. 1998, ARA&A, 36, 189
Kim, D., Im, M., & Kim, M. 2010, ApJ, 724, 386
Komarova, L., Oey, M. S., Hernandez, S., et al. 2024, ApJ, 967, 117
Koyama, Y., Shimakawa, R., Yamamura, I., Kodama, T., & Hayashi, M. 2018, PASJ, 71, 8
Kroupa, P. 2001, MNRAS, 322, 231
Leitherer, C., Schaerer, D., Goldader, J. D., et al. 1999, ApJS, 123, 3
Lintott, C., Schwamb, M., Fischer, D., et al. 2012, AAS Meeting, 219, 125.07
Liu, G., Calzetti, D., Kennicutt, R. C., Jr., et al. 2013, ApJ, 772, 27
Liu, Z., Morishita, T., & Kodama, T. 2024, arXiv:2406.11188
Lorenz, B., Suess, K. A., Kriek, M., et al. 2025, ApJL, 988, L20
Luo, B., Brandt, W. N., Xue, Y. Q., et al. 2017, ApJS, 228, 2
Lyu, J., Alberts, S., Rieke, G. H., et al. 2024, ApJ, 966, 229
Magnelli, B., Ivison, R. J., Lutz, D., et al. 2015, A&A, 573, A45
Matthews, A. M., Condon, J. J., Cotton, W. D., & Mauch, T. 2021, ApJ, 914, 126
Mauduit, J. C., Lacy, M., Farrah, D., et al. 2012, PASP, 124, 714
McAlpine, K., Jarvis, M. J., & Bonfield, D. G. 2013, MNRAS, 436, 1084
Minezaki, T., Kato, D., Sako, S., et al. 2010, SPIE, 7733, 773356
Mohan, N., & Rafferty, D. 2015, PyBDSF: Python Blob Detection and Source Finder, Astrophysics Source Code Library, 1502.007
Molnár, D. C., Sargent, M. T., Leslie, S., et al. 2021, MNRAS, 504, 118
Motohara, K., Mitani, N., Sako, S., et al. 2008, SPIE, 7014, 70142T
Muratov, A. L., Kereš, D., Faucher-Giguère, C.-A., et al. 2015, MNRAS, 454, 2691
Murphy, E., Carilli, C., Armus, L., et al. 2019, BAAS, 51, 471
Murphy, E. J., Condon, J. J., Schinnerer, E., et al. 2011, ApJ, 737, 67
Murphy, T. W., Jr., Soifer, B. T., Matthews, K., Kiger, J. R., & Armus, L. 1999, ApJL, 525, L85
Neufeld, C., van Dokkum, P., Asali, Y., et al. 2024, ApJ, 972, 156
Novak, M., Smolčić, V., Delhaize, J., et al. 2017, A&A, 602, A5
Oesch, P. A., Brammer, G., Naidu, R. P., et al. 2023, MNRAS, 525, 2864
Osterbrock, D. 1989, The Astrophysics of Gaseous Nebulae and Active Galactic Nuclei (Univ. Science Books)
Prandoni, I., & Seymour, N. 2015, in Advancing Astrophysics with the Square Kilometre Array (AASKA14) (SISSA), 67
Reddy, N. A., Shapley, A. E., Sanders, R. L., et al. 2025, arXiv:2506.17396
Reddy, N. A., Topping, M. W., Sanders, R. L., Shapley, A. E., & Brammer, G. 2023, ApJ, 948, 83
Rieke, G., Alberts, S., Lyu, J., Morrison, J., & Shivaei, I. 2017, MIRI in the Hubble Ultra-Deep Field, JWST Proposal. Cycle 1, ID. #1207,
Rubin, R. H. 1968, ApJ, 154, 391
Sanders, D. B., Mazzarella, J. M., Kim, D.-C., Surace, J. A., & Soifer, B. T. 2003, AJ, 126, 1607
Seymour, N., Dwelly, T., Moss, D., et al. 2008, MNRAS, 386, 1695
Seymour, N., McHardy, I. M., & Gunn, K. F. 2004, MNRAS, 352, 131
Skelton, R. E., Whitaker, K. E., Momcheva, I. G., et al. 2014, ApJS, 214, 24
Sun, Y., Lyu, J., Rieke, G. H., et al. 2025, ApJ, 978, 98
Sutherland, W., & Saunders, W. 1992, MNRAS, 259, 413
Symeonidis, M., Georgakakis, A., Seymour, N., et al. 2011, MNRAS, 417, 2239
Tabatabaei, F., Khademi, M., Jarvis, M. J., et al. 2025, ApJ, 989, 44
Tabatabaei, F. S., Schinnerer, E., Krause, M., et al. 2017, ApJ, 836, 185
Tateuchi, K., Konishi, M., Motohara, K., et al. 2015, ApJS, 217, 1
van der Vlugt, D., Algera, H. S. B., Hodge, J. A., et al. 2021, ApJ, 907, 5
van der Wel, A., Franx, M., van Dokkum, P. G., et al. 2014, ApJ, 788, 28
Wang, E., & Lilly, S. J. 2020, ApJ, 892, 87
Weston, S. D., Seymour, N., Gulyaev, S., et al. 2018, MNRAS, 473, 4523
Whittam, I. H., Jarvis, M. J., Murphy, E. J., et al. 2025, MNRAS, 543, 507
Whittam, I. H., Prescott, M., Hale, C. L., et al. 2024, MNRAS, 527, 3231
Williams, W. L., Hardcastle, M. J., Best, P. N., et al. 2019, A&A, 622, A2
Windhorst, R. A., van Heerde, G. M., & Katgert, P. 1984, A&AS, 58, 1
Yoshii, Y., Aoki, T., Doi, M., et al. 2010, SPIE, 7733, 773308
Yun, M. S., Reddy, N. A., & Condon, J. J. 2001, ApJ, 554, 803